NGC 2264 Cone Region Extremely High-Velocity Molecular Outflow Postprint

Authors: LIU Xinrong, LI Jingjing, LIU Dejian, KONG Deyun, LI Yingjie, LIN Zehao, HAO Chaojie, BIAN Shuaibo

Date: 2025-06-16T14:58:43+00:00

Abstract

Using high-sensitivity, high-resolution mapping observations of the 12CO (J = 1–0, J is the angular momentum quantum number) molecular line obtained with the 13.7 m millimeter-wave telescope at the Purple Mountain Observatory Qinghai Station, extremely high-velocity gas with a total velocity width of approximately 60 km · s^{-1} was discovered for the first time in the two sub-regions Spokes and Cone (C) of NGC 2264 Cone. The velocities of the detected outflows were divided into three velocity components (low-velocity, high-velocity, and extremely high-velocity) to reveal variations in the morphology and distribution of the molecular outflows. The extremely high-velocity 12CO emission exhibits multiple blue and red lobes, and as the gas velocity increases, the distance between the blue and red lobes increases significantly, showing a trend of outward motion. Physical parameters related to outflows of different velocities in the Cone region were calculated, and the results show that the low-velocity gas possesses the greatest amount of energy and luminosity. By comparing the total energy and total luminosity of the molecular outflows with the turbulent energy and luminosity of the molecular cloud, it is found that the molecular outflows in the Cone region may be an important factor affecting the turbulence of the molecular cloud.

Full Text

Preamble

Vol. 66 No. 3

May, 2025

Acta Astronomica Sinica

doi: 10.15940/j.cnki.0001-5245.2025.03.012

The Extremely High Velocity Molecular Outflow in the NGC 2264 Cone Region

LIU Xin-rong[1],[2], LI Jing-jing[1]†, LIU De-jian[1],[2], KONG De-yun[1],[2], LI Ying-jie[1], LIN Ze-hao[1], HAO Chao-jie[1], BIAN Shuai-bo[1]

[1] Purple Mountain Observatory, Chinese Academy of Sciences, Nanjing 210023
[2] School of Astronomy and Space Sciences, University of Science and Technology of China, Hefei 230026

Abstract

Using high-sensitivity, high-resolution mapping observations of the 12CO (J = 1−0, where J is the angular momentum quantum number) molecular line obtained with the 13.7 m millimeter-wave telescope at the Qinghai Observatory of Purple Mountain Observatory, we have for the first time discovered extremely high velocity gas with total velocity widths of approximately 60 $\mathrm{km \cdot s^{-1}}$ in the two sub-regions Spokes and Cone (C) of NGC 2264 Cone. The detected outflow velocities were divided into three velocity components (low, high, and extremely high velocity) to reveal variations in the morphology and distribution of the molecular outflows. The extremely high velocity 12CO emission displays multiple blueshifted and redshifted lobes, with the separation between blueshifted and redshifted lobes increasing significantly as the gas velocity increases, indicating an outward motion trend. We calculated the relevant physical parameters for outflows at different velocities in the Cone region, and the results show that low-velocity gas possesses the greatest amount of energy and luminosity. By comparing the total energy and luminosity of the molecular outflows with the turbulent energy and luminosity of the molecular cloud, we find that the molecular outflows in the Cone region may be an important factor influencing the turbulence of the molecular cloud.

Keywords ISM: outflows, ISM: clouds, stars: formation, stars: activity

1 Introduction

During star formation, when molecular clouds collapse due to gravitational instability, magnetohydrodynamic-driven winds erupt from the rotation axes of protostar-disk systems, entraining surrounding gas and accelerating it to velocities exceeding those of the molecular cloud, thereby forming molecular outflows. Molecular outflows play an indispensable role in the evolution of young stars: on one hand, they eject material and transfer excess angular momentum accumulated during mass infall, facilitating further contraction of molecular cloud cores; on the other hand, they inject energy into the surrounding medium, which can inhibit star formation. These two competing processes regulate star formation. Molecular outflows not only play a crucial role during protostar formation but also have significant impacts on their surrounding environments. High-energy molecular outflows can inject momentum and energy

into the surrounding medium, potentially dispersing nearby gas and generating turbulent motions. Particularly in low-mass star-forming regions, outflows may disrupt the local environment and limit the lifetime of their parent molecular clouds. Analytical and numerical studies have shown that outflows can interact with molecular clouds and effectively drive turbulent motions within the parent cloud. However, other studies suggest that while outflows can destroy dense clumps and affect molecular cloud structure, they have relatively little impact on turbulence within the cloud.

Zuckerman et al. first discovered high-velocity molecular outflows in the Orion molecular cloud in 1976 using 12CO (J=1−0) observations, with total velocity widths exceeding 150 $\mathrm{km \cdot s^{-1}}$. Subsequent studies revealed that molecular outflows are ubiquitous during star formation, observed in both low-mass and high-mass star-forming regions, and even detected in brown dwarf formation regions. Over the past several decades, improvements in telescope resolution and sensitivity have enabled large-scale searches for molecular outflows in molecular cloud regions, dramatically increasing the outflow sample and greatly enhancing our understanding of these phenomena. Some studies have revealed relationships between molecular outflows and the properties of their driving sources. For instance, investigations of massive star outflows by Shepherd et al., Henning et al., Zhang et al., and Ridge et al. found that approximately 90% of massive star-forming regions are associated with high-velocity gas. Other studies have directly measured the turbulent energy injected by molecular outflows into their parent clusters, demonstrating that the energy input from outflows can be comparable to the turbulent or gravitational binding energy of molecular clouds. However, a clear and coherent picture of molecular outflow evolution has yet to emerge.

CO is the most abundant molecule in the interstellar medium after H_2 and He. With its small spontaneous emission coefficient, CO can be excited through collisions even at relatively low densities, making the CO (J=1−0) transition an excellent tracer of molecular gas. Currently, CO (J=1−0) observations are widely used to study star-forming regions, providing valuable information about the morphology and physical properties of molecular clouds. Shepherd et al. classified massive star-forming regions into different types based on the total width (FW) of 12CO (J=1−0) lines: low-velocity sources (FW < 15 $\mathrm{km \cdot s^{-1}}$), intermediate-velocity sources (15 $\mathrm{km \cdot s^{-1}} \leq$ FW < 30 $\mathrm{km \cdot s^{-1}}$), high-velocity sources (30 $\mathrm{km \cdot s^{-1}} \leq$ FW < 45 $\mathrm{km \cdot s^{-1}}$), and extremely high-velocity sources (FW ≥ 45 $\mathrm{km \cdot s^{-1}}$). Different velocity components exhibit distinctly different spatial distributions and physical properties. Chernin et al. showed that extremely high-velocity CO gas is more collimated and hotter than low-velocity CO gas, and that extremely high-velocity CO outflows are produced through interactions between the parent molecular cloud and jets. In most cases, molecular outflows are dominated by low-velocity gas, with only a small fraction being dominated by extremely high-velocity gas, which appears to be associated with the youngest protostars and represents high-energy material ejection during early stellar evolution.

Extremely high-velocity molecular outflows have attracted considerable attention from researchers. Studies of these outflows became active in the 1980s, with early theories suggesting they likely consisted of parent cloud material accelerated by protostellar winds. However, studies of ionized winds driving high-velocity gas found insufficient momentum to entrain molecular cloud material, leading many to postulate the role of neutral winds, which were subsequently detected through HI 21 cm line observations around some sources. Lizano et al. detected HI winds in HH7-11 and proposed that neutral winds could drive molecular outflows. Koo and Margulis et al. also identified extremely high-velocity wings in CO spectra of several sources, suggesting that winds might contain CO. More recently, Li et al. found that HI winds can also drive molecular outflows in massive star-forming regions. Regarding models of extremely high-velocity gas, the "unified model" proposed by Shang et al. is particularly noteworthy. Their simulations of interactions between stellar winds and surrounding dense gas demonstrated that outflow shells originate from ambient gas compressed by wide-angle winds, while jet-like extremely high-velocity gas represents the most collimated central portion of the wind itself.

NGC 2264 is an excellent target for studying the formation of extremely high-velocity outflows. Located at a distance of only 727 pc (as estimated from Gaia parallaxes by Flaccomio et al.), with low foreground extinction and numerous pre-main-sequence stars, it is famous for the Cone Nebula. The Cone Nebula hosts active star formation, with many embedded Class 0/I protostars detected in submillimeter continuum observations. Approximately 0.7 pc north of the Cone Nebula, Allen discovered a bright embedded infrared source called IRS1, associated with IRAS 06384+0932 and also known as Allen's source, with a luminosity of 2000 L and mass of 10 M . About 1.4 pc northwest of IRS1 lies another IRAS source, IRAS 06382+0939, also called IRS2, which is a Class I young star with luminosity of 400 L and mass of 8 M . Both IRS1 and IRS2 are associated with molecular outflows. Sung et al. analyzed Spitzer photometric data for NGC 2264, mapping the spatial structure and exploring possible sub-clusters. Based on the spatial distribution of cluster members and their relationship to disk or envelope properties, they identified two active star-forming regions: S Mon in the north of NGC 2264 and the Cone region near the tip of the Cone Nebula in the south. Furthermore, Sung et al. divided the Cone region into two sub-regions: the Spokes cluster and Cone (C), where Cone (C) is the core of the Cone Nebula.

shows the integrated intensity map of the entire NGC 2264 region, with the white box indicating our focus area for subsequent analysis.

2 Data

We conducted 12CO, 13CO, and C18O (J=1−0) line observations of the region covering l = 203.1°–203.5°, b = 1.8°–2.3° using the 13.7 m millimeter-wave telescope at the Qinghai Observatory of Purple Mountain Observatory. The telescope receiver is a Superconducting Spectroscopic Array Receiver (SSAR)

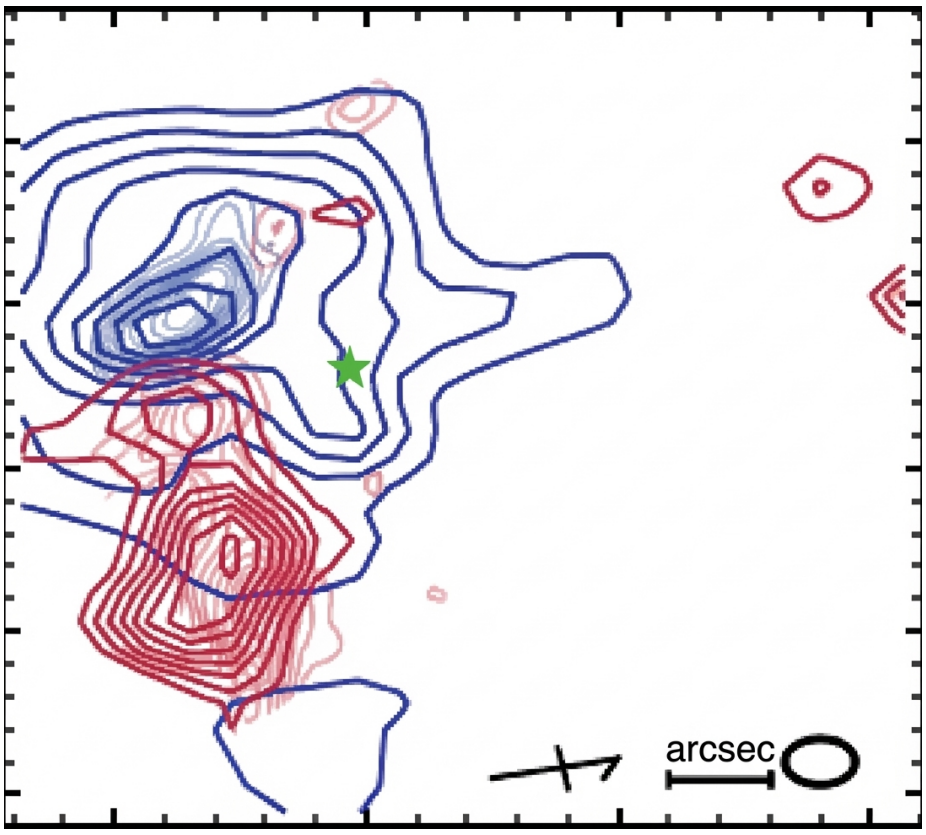

Figure 1: Figure 1

with 3 × 3 beams, employing sideband-separating superconductor-insulator-superconductor (SIS) mixers capable of simultaneously observing 12CO, 13CO, and C18O line emission. The 12CO (J=1−0) line is in the upper sideband with a system noise temperature of 250–300 K, while the 13CO (J=1−0) and C18O lines are in the lower sideband with system noise temperatures of 150–200 K. Each sideband backend employs a Fast Fourier Transform Spectrometer (FFTS) for real-time spectral processing, with a total bandwidth of 1 GHz divided into 16384 frequency channels. Each channel has a frequency resolution of 61 kHz, corresponding to a velocity range of 2600 $km \cdot s^{-1}$ and velocity resolutions of 0.16 $km \cdot s^{-1}$ at 115 GHz and 0.17 $km \cdot s^{-1}$ at 110 GHz.

We observed the region using On-The-Fly (OTF) mapping mode in equatorial coordinates. All raw data were processed using the Class package within GILDAS (Grenoble Image and Line Data Analysis Software). We fitted the 12CO spectra with the lowest-order polynomial (typically linear) and resampled the original OTF data onto pixels in Galactic longitude and latitude through convolution with a Gaussian function, finally converting to three-dimensional Flexible Image Transport System (FITS) files. All results in this paper are presented as main beam brightness temperature (Tmb), corrected from antenna temperature (TA) using Tmb = TA/ mb, where mb is the main beam efficiency obtained from the telescope's seasonal status reports. Basic parameters of the molecular lines are listed in Table 1 , including Molecular line (species), Rest frequency, HPBW (Half-Power Beam Width), Tsys (system temperature), and Δv (velocity per channel).

Previous studies of the Cone region revealed high-velocity bipolar outflows with total line widths FW < 40 $km \cdot s^{-1}$. This work utilizes 12CO (J=1−0) observations to extend the line wings to extremely high velocities (FW > 45 $km \cdot s^{-1}$), representing the first detection of extremely high-velocity bipolar outflows in the Cone region. The paper is organized as follows: Section 2 describes the performance of the Delingha 13.7 m telescope and observational data; Section 3 presents the morphological structure of molecular outflows in the Cone region, separately describing the Spokes and Cone (C) regions; Section 4 discusses the physical properties of the Cone region outflows; Section 5 examines the energy feedback from molecular outflows to the parent molecular cloud; and Section 6 summarizes the findings.

Koo and Margulis et al. found that high-velocity emission typically becomes detectable only when brightness temperatures fall below 100 mK. To reduce root mean square (rms) noise interference, velocity channels were smoothed to 1 $km \cdot s^{-1}$. [FIGURE:2] shows the spatial distribution of rms noise for 12CO in the Cone region, with noise levels ranging from 0 to 0.05 K.

3 Morphological Characteristics of Molecular Outflows

We employed a method combining comparison of 12CO and 13CO spectra at peak positions (Figure 3 [FIGURE:3]) with velocity channel maps (see Appendix

A1) to divide the 12CO line wings into different velocity ranges based on the total line width at the 1 rms (σ) level. These were categorized as low-velocity (LV), high-velocity (HV), and extremely high-velocity (EHV) components. Separating lower-velocity from higher-velocity gas in outflows allows better definition of high-velocity gas kinematics, and this represents the first detection of extremely high-velocity molecular outflows in the Cone region using high-sensitivity data. Figures 3(b)–(i) display the 12CO (J=1−0) and 13CO (J=1−0) spectra at emission peak positions of blueshifted and redshifted lobes in the Cone region, with velocity ranges indicated by dashed lines and summarized in Table 2 , which lists the velocity ranges for blueshifted and redshifted lobes.

Figure 3(a) shows the bipolar outflow structure of 12CO (J=1−0) in the Cone region (without distinguishing between LV, HV, and EHV components). The region contains two bipolar outflows: one in the Cone (C) region extending in the southeast-northwest direction (dashed line 1), and another in the Spokes region extending in the northeast-southwest direction (dashed line 2). The Cone (C) outflow has blueshifted velocities of −16 to 0 $\mathrm{km \cdot s^{-1}}$ and redshifted velocities of 10 to 39 $\mathrm{km \cdot s^{-1}}$, while the Spokes outflow has blueshifted velocities of −24 to 3 $\mathrm{km \cdot s^{-1}}$ and redshifted velocities of 10 to 35 $\mathrm{km \cdot s^{-1}}$. The figure clearly shows that the blueshifted and redshifted lobes of the Spokes outflow are more extended than those of the Cone (C) outflow. The angular sizes of both lobes in the Spokes region are 360 , corresponding to an effective radius of 1.25 pc, whereas the southeast-northwest lobes have angular sizes of 144 , corresponding to an effective radius of 0.5 pc.

3.1 Morphological Characteristics of the Spokes Region Outflow

Figure 4 [FIGURE:4] presents the LV, HV, and EHV components of the 12CO (J=1−0) outflow structure in the Spokes region, with velocity ranges listed in Table 2. The Spokes outflow exhibits clear bipolar characteristics across all velocity intervals, with spatially separated redshifted and blueshifted lobes visible in each. A systematic trend is evident: as outflow velocity increases, the redshifted lobe extends progressively northwestward, and the separation between blueshifted and redshifted lobes increases accordingly. Lada et al. observed the same kinematic trend in their JCMT 12CO (J=2−1) study of the NGC 2264G region outflow.

Figure 4(a) shows the distribution of low-velocity outflow, with blueshifted velocities of −4 to 3 $\mathrm{km \cdot s^{-1}}$ and redshifted velocities of 10 to 18 $\mathrm{km \cdot s^{-1}}$. The low-velocity outflow has a bipolar structure extending east-west. The blueshifted and redshifted lobes are spatially separated, with the blueshifted lobe distributed primarily in the eastern part of the molecular clump as a spreading blocky structure, while the redshifted lobe is concentrated in the west, extending northeast-southwest. The spatial structure resembles that shown in Figure 3(a) (which includes LV, HV, and EHV components) along the northeast-southwest direction, but the low-velocity lobes cover a smaller area.

Figure 4(b) shows the high-velocity outflow distribution, with blueshifted velocities of −14 to −4 km · s^{-1} and redshifted velocities of 18 to 27 km · s^{-1}. The high-velocity outflow has a more complex structure, consisting of one blueshifted lobe and two redshifted lobes located to the west and northeast of the blueshifted lobe. The blueshifted lobe appears as a north-south elongated ellipse. A redshifted lobe extending northeast-southwest (dashed line 1) is detected in the high-velocity outflow but is absent at that position in the low-velocity outflow. The east-west extending redshifted lobe (dashed line 2) contains two emission peaks at positions (l = 203.3°, b = 1.96°) and (l = 203.24°, b = 2.01°). Compared to the low-velocity redshifted lobe, this east-west lobe extends farther west by approximately 0.5 pc.

Figure 4(c) shows the extremely high-velocity outflow distribution. For the first time using high-sensitivity data, we have detected extremely high-velocity blueshifted and redshifted lobes in the Spokes region, with velocities of −24 to −14 km · s^{-1} and 27 to 35 km · s^{-1}, respectively. The extremely high-velocity outflow has the most extended structure, comprising one blueshifted lobe and two redshifted lobes located to the northwest and northeast of the blueshifted lobe. The extremely high-velocity blueshifted lobe has a similar morphology to the high-velocity blueshifted lobe but covers a smaller area. The extremely high-velocity redshifted lobe extending northeast-southwest (dashed line 3) is located at the emission peak position of the high-velocity redshifted lobe and may represent a remnant of the high-velocity outflow. The extremely high-velocity redshifted lobe to the northeast of the blueshifted lobe (dashed line 4) extends northeast-southwest, appearing northwest of the low-velocity redshifted lobe's terminus where little low-velocity gas is present. Compared to the east-west redshifted lobe in the high-velocity outflow, this extremely high-velocity redshifted lobe has shifted northward by 0.5 pc and is farther from the blueshifted lobe, indicating that the molecular outflow becomes more extended at extremely high velocities and moves progressively outward as velocity increases.

Shimoikura et al. used 12CO (J=1−0) mapping observations with 66 angular resolution and 1.2 K noise level to detect only a low-velocity blueshifted lobe in the Spokes region with velocities of −9 to 1 km · s^{-1}. Kim et al. observed 12CO (J=2−1) with the NRAO 12 m telescope at 45 resolution, 0.68 km · s^{-1} velocity resolution, and 0.2 K rms, finding a bipolar outflow structure in the Spokes region with blueshifted velocities of −10.3 to 0.1 km · s^{-1} and redshifted velocities of 10.5 to 20.3 km · s^{-1}. Margulis et al. used NRAO 12 m and FCRAO 14 m telescopes with spatial resolutions of 22 and 27 , respectively, and rms of 0.1–0.3 K to detect a molecular outflow in the Spokes region with blueshifted velocities of −10 to 2 km · s^{-1} and redshifted velocities of 11 to 21 km · s^{-1}. To more clearly demonstrate the differences between the outflow morphology detected with the Delingha telescope's 12CO (J=1−0) line and previous studies, we overlay our detected outflow on the outflow maps from Kim et al. and Margulis et al. (Figures 5 [FIGURE:5] and 6 [FIGURE:6]).

Figure 5 shows the background outflow structure in the Spokes region detected

by Kim et al. in 12CO (J=2−1), with our 12CO (J=1−0) outflow contours overlaid. The figure reveals some morphological differences between the two molecular lines. The overall morphology of the blueshifted and redshifted lobes detected in 12CO (J=1−0) is more extended than that in 12CO (J=2−1), particularly along the short axes of the lobes. The 12CO (J=2−1) blueshifted lobe extends northeast-southwest and is concentrated near the peak position of the 12CO (J=1−0) blueshifted lobe. The 12CO (J=2−1) redshifted lobe extends east-west, with its peak position shifted northwest relative to the 12CO (J=1−0) redshifted lobe peak. These apparent morphological differences between 12CO (J=2−1) and 12CO (J=1−0) suggest that these lines trace different environmental gas components. Figure 6 shows the background blueshifted (dashed lines) and redshifted (solid lines) lobes around IRS2 drawn by Margulis et al., with our detected outflow overlaid. The outflow detected with the Delingha telescope shows similar morphological distribution to that of Margulis et al., though their detected blueshifted and redshifted lobes cover a broader area, likely due to different velocity range selections for the 12CO (J=1−0) line wings.

3.2 Morphological Characteristics of the Cone (C) Region Outflow

Figure 7 [FIGURE:7] shows the 12CO (J=1−0) outflow structure in the Cone (C) region for low, high, and extremely high velocities. Figure 7(a) presents the low-velocity outflow structure, with blueshifted velocities of −6 to 0 $\mathrm{km \cdot s^{-1}}$ and redshifted velocities of 10 to 20 $\mathrm{km \cdot s^{-1}}$. The low-velocity outflow exhibits bipolar characteristics, with a spherical blueshifted lobe and a northeast-southwest extended redshifted lobe. Partial overlap between the lobes may result from projection effects. Figure 7(b) shows the high-velocity outflow structure, with blueshifted velocities of −16 to −6 $\mathrm{km \cdot s^{-1}}$ and redshifted velocities of 20 to 25 $\mathrm{km \cdot s^{-1}}$. The high-velocity outflow consists of three blueshifted lobes—one east of the redshifted lobe extending east-west (dashed line 1), one southwest of the redshifted lobe (dashed line 2), and one extending northwest-southeast (dashed line 3)—and one redshifted lobe. Compared to the low-velocity redshifted lobe, the high-velocity redshifted lobe elongates north-south, becoming elliptical. Figure 7(c) shows the extremely high-velocity outflow structure, detecting only two redshifted lobes extending north-south (dashed line 4) and east-west (dashed line 5) with velocities of 25 to 39 $\mathrm{km \cdot s^{-1}}$. Compared to the high-velocity redshifted lobe, the north-south extremely high-velocity redshifted lobe (dashed line 5) becomes more elongated.

Margulis et al. used NRAO 12 m and FCRAO 14 m telescopes to detect a 12CO redshifted lobe in the Cone (C) region with velocities of 12–22 $\mathrm{km \cdot s^{-1}}$, an effective length of 0.24 pc, and no detected blueshifted lobe. Liu et al. used 12CO (J=1−0) observations with 47.4 mK rms to identify a bipolar outflow in this region, but the blueshifted lobe was not prominent, with velocities of −7 to 0 $\mathrm{km \cdot s^{-1}}$ for the blueshifted lobe and 12–22 $\mathrm{km \cdot s^{-1}}$ for the redshifted lobe. Thanks to the high-sensitivity observations with the Delingha telescope at the Qinghai Observatory, we have successfully detected clear high-velocity

and extremely high-velocity outflows in the Cone (C) region for the first time.

4 Physical Properties of Molecular Outflows

Understanding the impact of molecular outflows on their surroundings requires calculating outflow mass, momentum, and energy. However, as Arce et al. demonstrated, these calculations involve uncertainties. One major issue is confusion between the low-velocity portion of outflows and core gas not associated with the outflow. By examining the velocity range of 13CO (J=1−0) emission, we attempt to minimize contamination from ambient gas by simply eliminating low-velocity molecular gas emission, meaning our calculated outflow masses and energies represent lower limits. Another major uncertainty in determining outflow physical properties is the difficulty in determining the inclination angle of outflow ejection; therefore, we present outflow physical parameters without inclination corrections.

Tables 3 and 4 summarize the physical properties of outflows in the Spokes and Cone (C) regions, where M is outflow mass, P is momentum, E is energy, L is mechanical luminosity, and t is dynamical timescale. Lblue/red represents low-velocity blueshifted/redshifted lobes, Hblue/red represents high-velocity blueshifted/redshifted lobes, and Eblue/red represents extremely high-velocity blueshifted/redshifted lobes. Detailed calculations are described in Appendix A2. It should be noted that the masses, momenta, energies, and mechanical luminosities listed in Tables 3 and 4 are lower limits, as some influencing factors have not been considered; incorporating these factors would increase these parameters.

The data show that Spokes region outflow masses range from 0.01 to 3.39 M , momenta from 0.21 to 13.45 M $\cdot$ km $\cdot$ s^{-1}, energies from 0.51$×10^{44}$ to 9.18$×10^{44}$ erg, luminosities from 0.05 to 0.41 L , and dynamical timescales from 0.5$×10^{4}$ to 8.5$×10^{4}$ yr. Cone (C) region outflow masses range from 0.01 to 3.38 M , momenta from 0.06 to 20.55 M $\cdot$ km $\cdot$ s^{-1}, energies from 0.08$×10^{44}$ to 13.71$×10^{44}$ erg, luminosities from 0.01 to 0.74 L , and dynamical timescales from 0.5$×10^{4}$ to 1.5$×10^{4}$ yr. Low-velocity, high-velocity, and extremely high-velocity outflows have similar mechanical luminosities. However, most mass, momentum, and energy are concentrated in the low-velocity regime, while extremely high-velocity outflows contain the least mass, momentum, and energy. Quantitatively, extremely high-velocity outflows in the Spokes region contain only 1% of the mass, 5% of the momentum, and 16% of the energy, while those in the Cone (C) region contain only 1% of the mass, 3% of the momentum, and 8% of the energy. Low-velocity outflows in both regions carry the vast majority of mass, momentum, and energy. The dynamical timescales satisfy t_{EHV} < t_{HV} < t_{LV}, indicating that extremely high-velocity outflows are the youngest. Additionally, we find that redshifted lobes in both Spokes and Cone (C) regions contain more momentum and energy than blueshifted lobes. Buckle et al. also found that redshifted lobes contain more momentum and energy in their CO study of NGC 2264 outflows.

5 Impact of Molecular Outflows on Molecular Clouds

Over the past 30 years, turbulent motions in molecular clouds have remained controversial. On large scales, kinetic energy from supernovae and galactic differential rotation can provide turbulent energy, while on small scales, stellar feedback from H II regions, radiation-driven winds, and radiation-accreting outflows are the main sources of turbulent energy. Theoretical and numerical studies have shown that outflows can effectively drive turbulent motions in molecular clouds. In small-scale molecular clouds, energy injected by outflows can compensate for rapid turbulent dissipation within several dynamical timescales. In Nakamura et al.'s models, outflows balance infall and accretion motions in molecular clouds, maintaining them in quasi-static equilibrium. Without additional turbulent motions injected by outflows, turbulence would dissipate within a few free-fall timescales. Therefore, molecular outflows may prevent local gravitational collapse of molecular clouds, thereby extending their lifetimes.

Generally, outflow feedback on parent molecular clouds is studied from two perspectives: turbulent support and cloud disruption. The impact of outflows on cloud turbulence is typically evaluated by comparing total outflow energy with the turbulent energy of the parent cloud. For example, Graves et al. found that outflow energy in the Serpens molecular cloud is 70% of its turbulent energy, while Arce et al. identified 60 outflow candidates in Serpens and concluded that total outflow energy is sufficient to compensate for turbulent dissipation. Similar results have been found in Taurus, Ophiuchus, and Orion. Li et al. studied turbulent support and disruption by outflows in 265 molecular clouds, finding that outflows can maintain turbulence on relatively small scales and even disrupt clouds.

To estimate the contribution of outflows to turbulence in the Cone region molecular cloud, we compare total molecular outflow energy with molecular cloud turbulent energy, focusing on three aspects: total outflow energy versus cloud turbulent energy, total outflow luminosity (total energy injection rate) versus turbulent luminosity (energy dissipation rate), and total outflow kinetic energy versus cloud gravitational binding energy.

We use 13CO to calculate molecular cloud physical properties. In regions with C18O emission, we calculate optical depth from C18O data and convert to 13CO optical depth using abundance ratios. In regions without C18O emission, we use 13CO optical depth directly. We then apply optical depth corrections to gas column densities for subsequent calculations of cloud physical quantities.

Assuming optically thick 12CO (J=1−0) emission, the excitation temperature is given by:

$$T_{ex} = 5.53/\ln\left[1 + 5.53/(T_{mb,12} + 0.82)\right] \quad (1)$$

where Tmb,12 is the 12CO main beam temperature. In regions with C18O

emission, we estimate the C18O optical depth using the 12CO excitation temperature:

$$\tau_{18} = -\ln\left\{1 - T_{mb,18} \times 5.27\left[(e^{5.27/T_{ex}} - 1)^{-1} - 0.166\right]^{-1}\right\} \quad (2)$$

The corresponding 13CO optical depth is:

$$\tau_{13} = \tau_{18} \times X_{13/18} \quad (3)$$

where Tmb,18 is the C18O main beam temperature and X13/18 = [13CO/C18O] = 9.7 is the abundance ratio. In regions without C18O emission, we estimate 13CO optical depth using the 12CO excitation temperature:

$$\tau_{13} = -\ln\left\{1 - T_{mb,13} \times 5.29\left[(e^{5.29/T_{ex}} - 1)^{-1} - 0.164\right]^{-1}\right\} \quad (4)$$

Assuming local thermodynamic equilibrium (LTE), we use 13CO (J=1−0) to estimate molecular gas column density and mass. Following Garden et al., the 13CO column density after optical depth correction can be estimated by:

$$N(^{13}\mathrm{CO}) = 4.71 \times 10^{13} \frac{T_{ex} + 0.88}{e^{-5.29/T_{ex}}} \frac{\tau_{13}}{1 - e^{-\tau_{13}}} \int T_{mb,13}\, dv \quad (5)$$

The H_2 column density is estimated using the abundance ratio X(13CO) = $[H_2]/[13CO]$ 5×10^5, yielding the molecular cloud mass:

$$M_{\mathrm{cloud}} = \mu m_H N_{H_2} S \quad (6)$$

where = 2.8 is the mean molecular weight, m_H = 1.674×10^{-27} kg is the hydrogen atom mass, and S is the projected area of the molecular cloud on the sky.

From 13CO (J=1−0) observations of the Spokes and Cone (C) regions, we obtain average line widths Δv_{FWHM} of 3 km·s^{-1} and 4 km·s^{-1}, respectively. The turbulent energy of the molecular cloud is then:

$$E_{\mathrm{turb}} = \frac{3}{16} \ln 2\, M_{\mathrm{cloud}}\, \Delta v^2_{\mathrm{FWHM}} \quad (7)$$

To estimate the turbulent energy dissipation rate, we need the turbulent dissipation timescale. Numerical studies show that the energy dissipation rate for uniformly driven magnetohydrodynamic turbulence can be approximated by:

$$t_{\mathrm{diss}} \approx 3.9\, t_{\mathrm{ff}} \left(\frac{\lambda_{\mathrm{drive}}}{\lambda_J}\right) \quad (8)$$

where λ_{drive} is the driving wavelength (approximately equal to the outflow length), *λJ is the Jeans length of the molecular cloud, and t*{ff} is the free-fall timescale. The dissipation rate can be written as the ratio of turbulent energy to dissipation timescale:

$$L_{\rm turb} = E_{\rm turb}/t_{\rm diss} \quad (9)$$

Comparing total outflow kinetic energy with molecular cloud gravitational binding energy estimates the disruptive effect of outflows on clouds. The gravitational binding energy is:

$$E_{\rm grav} = \frac{GM_{\rm cloud}^2}{R_{\rm cloud}} \quad (10)$$

Table 5 summarizes the physical properties of the molecular clouds, where E_{flow} is the total outflow energy and L_{flow} is the total outflow luminosity. The outflow energies and luminosities in Table 5 are lower limits because inclination and blending corrections have not been applied. Accounting for blending factors would double the outflow mass. Assuming an average outflow inclination of 57.3°, velocities and dynamical timescales should be multiplied by 1.9 and 0.64, respectively. Combining blending and inclination correction factors, outflow momentum, energy, and luminosity should be multiplied by 3.8, 6.8, and 11, respectively. After correction, the Spokes region outflow has total energy and luminosity of 1.6×10^{46} erg and 5.4×10^{34} erg $\cdot$ s^{-1}, respectively, while the Cone (C) region outflow has total energy and luminosity of 1.2×10^{46} erg and 4.5×10^{34} erg $\cdot$ s^{-1}, respectively. The corrected data show that turbulent energies in both Spokes and Cone (C) regions exceed their respective outflow energies, indicating that total outflow energy cannot balance cloud turbulent energy. However, total outflow luminosities in both regions exceed their parent clouds' turbulent luminosities, demonstrating that outflows have sufficient energy injection rates to maintain turbulent dissipation. The ratio E_{flow}/E_{grav} is less than 10% in both regions, indicating that outflows are not yet energetic enough to destroy their host molecular clouds.

6 Summary

Using 12CO (J=1−0) observations from the Delingha 13.7 m millimeter-wave telescope at the Qinghai Observatory, we have studied the dynamical structure of molecular outflows in the Cone region. Benefiting from high-sensitivity mapping observations, we have for the first time detected extremely high-velocity molecular outflows in the Cone region and analyzed their impact on the molecular cloud. Our main findings regarding the dynamical structure and characteristics of the Cone region molecular cloud are:

1. The 12CO (J=1−0) line in the Spokes region shows zero-intensity velocity widths up to 59 km $\cdot$ s^{-1}, including three distinct velocity components:

low-velocity, high-velocity, and extremely high-velocity outflows. Based on 12CO (J=1−0), different velocity components in the Spokes region all exhibit bipolar characteristics, revealing a unique morphological evolution of molecular outflows.

2. The 12CO (J=1−0) line in the Cone (C) region shows zero-intensity velocity widths up to 55 $km \cdot s^{-1}$, compared to only 29 $km \cdot s^{-1}$ in previous studies. Bipolar molecular outflows are detected in both low-velocity and high-velocity gas, with the high-velocity gas containing three blueshifted lobes. Two redshifted lobes are detected in the extremely high-velocity gas.

3. As molecular outflow velocity increases, the separation between redshifted and blueshifted lobes gradually increases, showing a trend of outward motion. This is consistent with the outflow variation trend previously observed by Lada et al. in the NGC 2264G region using 12CO (J=2−1).

4. Assuming local thermodynamic equilibrium, we calculated physical properties including mass, momentum, kinetic energy, mechanical luminosity, and dynamical timescale for each outflow. We find that low-velocity gas contains more mass, momentum, and energy than extremely high-velocity gas. Additionally, redshifted lobes in both Spokes and Cone (C) regions contain more momentum and energy than blueshifted lobes.

5. By calculating molecular cloud dynamical parameters such as turbulent energy, turbulent dissipation rate, and gravitational binding energy, and comparing them with outflow energy and luminosity, we find that outflows in both Spokes and Cone (C) regions have sufficient energy injection rates to balance turbulent dissipation in the molecular clouds. However, the outflows do not have enough energy to maintain the currently observed cloud turbulence, and their kinetic energies are too small to disrupt the molecular clouds.

Acknowledgments

This work utilizes observational data from the Delingha 13.7 m millimeter-wave telescope. We thank the Qinghai Observatory of Purple Mountain Observatory for providing data support for this project. We also thank the referee for valuable suggestions that significantly improved the quality of this paper.

References

Arce H G, Borkin M A, Goodman A A, et al. ApJ, 2010, 715: 1170
Li Y J, Li F C, Xu Y, et al. ApJS, 2018, 235: 15
Li Y J, Xu Y, Sun Y, et al. ApJS, 2020, 251: 26
Bachiller R. ARA&A, 1996, 34: 111
Plunkett A L, Arce H G, Corder S A, et al. ApJ, 2013, 774: 22
Lada C J. ARA&A, 1985, 23: 267

Nakamura F, Li Z Y. ApJ, 2007, 662: 395
Cunningham A J, Frank A, Carroll J, et al. ApJ, 2009, 692: 816
Hartmann L, Ballesteros-Paredes J, Bergin E A. ApJ, 2001, 562: 852
Matzner C D. ApJ, 2007, 659: 1394
Carroll J J, Frank A, Blackman E G, et al. ApJ, 2009, 695: 1376
Banerjee R, Klessen R S, Fendt C. ApJ, 2007, 668: 1028
Zuckerman B, Kuiper T, Rodriguez K E. ApJL, 1976, 209: L137
Hatchell J, Fuller G A, Richer J S. A&A, 2007, 472: 259
Hatchell J, Dunham M M. A&A, 2009, 502: 139
Wu Y, Wei Y, Zhao M, et al. A&A, 2004, 426: 503
Phan B N, Riaz B, Lee C F, et al. ApJL, 2008, 689: L141
Li Y J, Xu Y, Sun Y, et al. ApJS, 2019, 242: 19
Cabrit S, Bertout C. A&A, 1992, 261: 274
Bontemps S, Andre P, Terebey S, et al. A&A, 1996, 311: 858
Curtis E I, Richer J S, Swift J J, et al. MNRAS, 2010, 408: 1516
Shepherd D S, Churchwell E. ApJ, 1996, 457: 267
Shepherd D S, Churchwell E. ApJ, 1996, 472: 225
Henning T H, Schreyer K, Launhard R, et al. A&A, 2000, 353: 211
Zhang Q, Hunter T R, Brand J, et al. ApJ, 2001, 552: 167
Ridge N A, Moore T J T. A&A, 2001, 378: 495
Ginsburg A, Bally J, Williams J P. MNRAS, 2011, 418: 2121
Nakamura F, Sugitani K, Shimajiri Y, et al. ApJ, 2011, 737: 56
Goldsmith P F, Heyer M, Narayanan G, et al. ApJ, 2008, 680: 428
Yonekura Y, Asayama S, Kimura K, et al. ApJ, 2005, 634: 476
Chernin L M, Masson C R. ApJ, 1992, 396: L35
André P, Ward-Thompson D, Barsony M. ApJ, 1993, 406: 122
Lizano S, Heiles C, Rodriguez L F, et al. ApJ, 1988, 328: 763
Koo B C. ApJ, 1989, 337: 318
Koo B C. ApJ, 1990, 361: 145
Sung H, Stauffer J R, Bessell M S. AJ, 2009, 138: 1116
Margulis M, Lada C J, Snell R L. ApJ, 1988, 333: 316
Liu D J, Xu Y, Li Y J, et al. ApJS, 2021, 253: 15
Kim K T, Kurtz S E. ApJ, 2006, 643: 978
Shan W, Yang J, Shi S, et al. ITTST, 2012, 2: 593
Sun J X, Lu D R, Yang J, et al. AcAer, 2018, 59: 3
Lada C J, Fich M. RMxAA, 1995, 1: 93
Shimoikura T, Dobashi K, Nakamura F, et al. ApJ, 2018, 855: 45
Margulis M, Snell R L. ApJ, 1989, 343: 779
Snell R L, Loren R B, Plambeck R L. ApJL, 1980, 239: L17
Arce H G, Goodman A. ApJL, 2001, 551: L171
Buckle J V, Richer J S, Davis C. NRAS, 2012, 423: 191
Evans N J, Levreault R M, Beckwith S, et al. ApJ, 1987, 320: 364
Li H, Li D, Qian L, et al. ApJS, 2015, 219: 20
Larson R B. MNRAS, 1981, 194: 809
Bally J, Predmore R. ApJ, 1983, 265: 778
Rodriguez L F, Cantó J. ApJ, 1983, 8: 163

Heyer M H, Brunt C M. ApJ, 2004, 615: L45
Narayanan G, Snell R, Bemis A. MNRAS, 2012, 425: 2687
Snell R L, Scoville N Z, Sanders D B, et al. ApJ, 1984, 284: 176
Graves S F, Richer J S, Buckle J V, et al. MNRAS, 2010, 409: 1412
Li Y J, Xu Y, Xu J L, et al. ApJL, 2022, 933: L26
Li Y J, Xu Y, Xu J L, et al. ApJ, 2022, 935: 153
Nakamura F, Kamada Y, Kamazaki T, et al. ApJ, 2011, 726: 46
Shang H, Allen A, Li Z Y, et al. ApJ, 2006, 649: 845
Flaccomio E, Micela G, Peres G, et al. A&A, 2023, 670: A79
Federrath C. MNRAS, 2015, 450: 4035
Garden R P, Hayashi M, Gatley I, et al. ApJ, 1991, 374: 540
Allen D. ApJ, 1972, 172: 55
Schwartz P R, Thronson H A, Odenwald S F, et al. ApJ, 1985, 292: 231
Wang C, Feng H R, Yang J, et al. AJ, 2023, 166: 121
Simon R, Jackson J M, Clemens D P, et al. ApJ, 2001, 551: 747
Schoettler C, Parker R J, de Bruijne J. MNRAS, 2022, 510: 3178
Kauffmann J, Bertoldi F, Bourke T L, et al. A&A, 2008, 487: 993
Peretto N, André P, Belloche A. A&A, 2006, 445: 979
Sung H, Bessell M S, Chun M Y, et al. AJ, 2008, 135: 441
Mac L, Mordecai M. ApJ, 1999, 542: 169

Appendix A1: Velocity Channel Maps of Molecular Outflows

Figure A.1 shows the velocity channel maps of the 12CO redshifted lobe in the Spokes region, with the background being the integrated intensity map of the 13CO molecular line. The velocity of each channel is displayed in the upper right corner of each panel. Contour levels for each channel's redshifted lobe range from 40% to 90% of that lobe's peak intensity. The beam size (black circle) and pc scale are shown in the lower right corner.

Figure A.2 shows the velocity channel maps of the 12CO blueshifted lobe in the Spokes region, with the background being the integrated intensity map of the 13CO molecular line. The velocity of each channel is displayed in the upper right corner of each panel. Contour levels for each channel's blueshifted lobe range from 40% to 90% of that lobe's peak intensity. The beam size (black circle) and pc scale are shown in the lower right corner.

Figure A.3 shows the velocity channel maps of the 12CO redshifted lobe in the Cone (C) region, with the background being the integrated intensity map of the 13CO molecular line. The velocity of each channel is displayed in the upper right corner of each panel. Contour levels for each channel's redshifted lobe range from 40% to 90% of that lobe's peak intensity. The beam size (black circle) and pc scale are shown in the lower right corner.

Figure A.4 shows the velocity channel maps of the 12CO blueshifted lobe in the Cone (C) region, with the background being the integrated intensity map

of the 13CO molecular line. The velocity of each channel is displayed in the upper right corner of each panel. Contour levels for each channel's blueshifted lobe range from 40% to 90% of that lobe's peak intensity. The beam size (black circle) and pc scale are shown in the lower right corner.

Appendix A2: Calculation Process for Molecular Outflow Physical Parameters

We use the method of Snell et al. to estimate outflow mass, assuming high-velocity gas is optically thin under local thermodynamic equilibrium conditions, with excitation temperature Tex = 30 K and abundance X(12CO) = [12CO]/[H_2] 10^{-4}. The H_2 column density traced by 12CO is:

$$N_{H_2} = 4.2 \times 10^{17} T_{ex} e^{-5.5/T_{ex}} \int T_{mb,12}\, dv \quad \text{(A.1)}$$

The outflow lobe mass is:

$$M_{\rm lobe} = \mu m_H A_{\rm lobe} N_{H_2} \quad \text{(A.2)}$$

where Ti is the main beam temperature in channel i, vi is the velocity corresponding to channel i, v_{peak} is the line center velocity, and Δv_{res} is the channel velocity resolution. Outflow momentum, energy, mechanical luminosity, and dynamical evolution timescale are:

$$\langle \Delta v_{\rm lobe} \rangle = \frac{\sum_i (v_i - v_{\rm peak}) T_i \Delta v_{\rm res}}{\sum_i T_i \Delta v_{\rm res}} \quad \text{(A.3)}$$

$$P_{\rm lobe} = \sum A_{\rm lobe} M_{\rm lobe} \langle \Delta v_{\rm lobe} \rangle \quad \text{(A.4)}$$

$$E_{\rm lobe} = \frac{1}{2} \sum A_{\rm lobe} M_{\rm lobe} \langle \Delta v^2_{\rm lobe} \rangle \quad \text{(A.5)}$$

$$L_{\rm lobe} = E_{\rm lobe} / t_{\rm lobe} \quad \text{(A.6)}$$

$$t_{\rm lobe} = l_{\rm lobe} / \Delta v_{\rm max} \quad \text{(A.7)}$$

where the integration covers the velocity ranges of line wings for blueshifted and redshifted lobes. The outflow gas mass is:

$$\langle \Delta v^2_{\rm lobe} \rangle = \frac{\sum_i (v_i - v_{\rm peak})^2 T_i \Delta v_{\rm res}}{\sum_i T_i \Delta v_{\rm res}}$$

The outflow lobe velocity (relative to the central core component) is calculated using:

where i and j are channel numbers for blueshifted and redshifted wings, respectively, A_{lobe} is the projected area of blueshifted and redshifted lobes on the sky (determined by the 50% intensity contour of lobe peaks), l_{lobe} is the outflow scale, and Δv_{max} is the maximum velocity of blueshifted and redshifted lobes.